



UNIVERSITY OF LEEDS

This is a repository copy of *A multifractal approach to space-filling recovery for PET quantification.*

White Rose Research Online URL for this paper:  
<http://eprints.whiterose.ac.uk/88657/>

Version: Accepted Version

---

**Article:**

Willaime, JMY, Aboagye, EO, Tsoumpas, C et al. (1 more author) (2014) A multifractal approach to space-filling recovery for PET quantification. *Medical Physics*, 41 (11). 112505. ISSN 0094-2405

<https://doi.org/10.1118/1.4898122>

---

**Reuse**

Unless indicated otherwise, fulltext items are protected by copyright with all rights reserved. The copyright exception in section 29 of the Copyright, Designs and Patents Act 1988 allows the making of a single copy solely for the purpose of non-commercial research or private study within the limits of fair dealing. The publisher or other rights-holder may allow further reproduction and re-use of this version - refer to the White Rose Research Online record for this item. Where records identify the publisher as the copyright holder, users can verify any specific terms of use on the publisher's website.

**Takedown**

If you consider content in White Rose Research Online to be in breach of UK law, please notify us by emailing [eprints@whiterose.ac.uk](mailto:eprints@whiterose.ac.uk) including the URL of the record and the reason for the withdrawal request.



[eprints@whiterose.ac.uk](mailto:eprints@whiterose.ac.uk)  
<https://eprints.whiterose.ac.uk/>

# A multifractal approach to space-filling recovery for PET quantification

Julien M.Y. Willaime <sup>a)</sup> and Eric O. Aboagye

Comprehensive Cancer Imaging Centre, Imperial College London, Hammersmith Hospital, London, W12 0NN, UK

5

Charalampos Tsoumpas

Division of Medical Physics, University of Leeds, LS2 9JT, UK

Federico E. Turkheimer

10 Department of Neuroimaging, Institute of Psychiatry, King's College London, London, SE5 8AF, UK

## Willaime *et al*: Space-filling index and PET quantification

**Purpose:** A new image-based methodology is developed for estimating the apparent space-filling  
15 properties of an object of interest in PET imaging without need for a robust segmentation step and used to  
recover accurate estimates of total lesion activity (TLA).

**Methods:** A multifractal approach and the fractal dimension are proposed to recover the apparent space-  
filling index of a lesion (tumor volume, TV) embedded in non-zero background. A practical  
implementation is proposed and the index is subsequently used with mean standardized uptake value  
20 ( $SUV_{\text{mean}}$ ) to correct TLA estimates obtained from approximate lesion contours. The methodology is  
illustrated on fractal and synthetic objects contaminated by partial volume effects (PVEs), validated on  
realistic  $^{18}\text{F}$ -fluorodeoxyglucose PET simulations and tested for its robustness using a clinical  $^{18}\text{F}$ -  
fluorothymidine PET test-retest dataset.

**Results:** TLA estimates were stable for a range of resolutions typical in PET oncology (4 to 6mm). By  
25 contrast, the space-filling index and intensity estimates were resolution dependent. TLA was generally  
recovered within 15% of ground truth on post-filtered PET images affected by PVEs. Volumes were  
recovered within 15% variability in the repeatability study. Results indicated that TLA is a more robust  
index than other traditional metrics such as  $SUV_{\text{mean}}$  or TV measurements across imaging protocols.

**Conclusions:** The fractal procedure reported here is proposed as a simple and effective computational  
30 alternative to existing methodologies which require the incorporation of image pre-processing steps (i.e.  
partial volume correction and automatic segmentation) prior to quantification.

Key words: fractal dimension, space-filling, total lesion activity, partial volume effects, PET,  
quantification

35

## **1. INTRODUCTION**

PET imaging is a powerful technique to quantify *in vivo* biological and biochemical alterations associated with diseases such as cancer. Standardized uptake values (SUVs), normalized measurements of radiotracer concentration in tissue, are most commonly used for PET quantification and treatment monitoring.<sup>1</sup> However, despite the introduction of standardization guidelines<sup>2</sup> a number of factors contribute to biases in quantification, including noise and partial volume effects (PVEs) in the reconstructed PET images. PVE designates a range of phenomena which result in cross-contamination of radiotracer activity between adjacent structures.<sup>3-5</sup> The main contribution to PVE comes from the finite spatial resolution of the imaging system due to PET physics (positron range, detectors, etc.), which results in a characteristic blur in the reconstructed images. Additional sources of PVE include voxel grid discretization, and image regularization (i.e. typical Gaussian image post-filtering). Typically, the mean SUV in a lesion ( $SUV_{\text{mean}}$ ) is affected by PVE, whilst  $SUV_{\text{max}}$ , computed from the single most intense voxel in the lesion, is sensitive to noise.  $SUV_{\text{peak}}$ , average SUV in a small volume of interest ( $VOI_{\text{peak}}$ ) centered on a high-uptake portion of the lesion, has been proposed as a more robust metric.<sup>6</sup> Functional tumor volume (TV) and total lesion activity (TLA)<sup>7, 8</sup> have also been used to characterize neoplastic lesions in PET imaging. TLA is a measure of total lesion burden computed as the product of TV and  $SUV_{\text{mean}}$ .

Typically, the computation of these indices relies on a lesion contouring step<sup>9, 10</sup> which PVEs render difficult because of diffuse lesion boundaries. It is important to note that PVEs do not imply a loss but rather a spatial redistribution of image intensities between neighboring voxels. In the simple case of a lesion in zero background, TLA is unchanged at different image resolutions.<sup>5</sup> A lowering of PET image resolution is also known to increase the apparent TV and decrease  $SUV_{\text{mean}}$ .<sup>11</sup> In this paper, the space-filling property of an object designates the way in which the object fills space (2D or 3D) at a given image resolution.

## Willaime *et al*: Space-filling index and PET quantification

60 We introduce a novel PET quantification methodology for recovering an apparent space-filling index (area or volume) of an object embedded in non-zero background without need for a robust segmentation step. Further, we use this space-filling index to correct  $SUV_{\text{mean}}$  and TLA estimates obtained from an approximate contouring of the object contaminated by PVEs. The method is based on a multifractal approach which is a generalization of fractal geometry to non-uniform objects.<sup>12-14</sup> The fractal dimension  
65 (FD)<sup>15</sup> is a non-integer index which provides a “scale-free” description of the space-filling properties of an object embedded in space of given topological dimension.<sup>16-18</sup> The closer the FD value is to the topological dimension, the more the object fills the space it is embedded in. Di Ieva *et al.*<sup>17</sup> proposed using the FD index as an indicative descriptor of the space-filling properties of tumor vasculature measured using ultra-high field MRI. Aschwanden *et al.*<sup>18</sup> derived a computation of the area of solar  
70 flares using FD. A fractal approach to capture the space-filling properties of breast lesions, using histology, has also been proposed to predict the evolution of cell density with tumor growth.<sup>19</sup> FD has been used in many fields, including medicine, to characterize the geometry of vascular networks and organ blood flow in relation to pathologies,<sup>16, 20, 21</sup> tumor boundaries<sup>22</sup> and the morphology of tumor cells.<sup>23</sup> Fractal geometry has also been applied to imaging modalities such as CT and MRI.<sup>24</sup> Goh *et al.*<sup>25</sup>  
75 explored morphological fractal analysis to assess colorectal tumor perfusion measured with CT on thresholded images, as well as its reproducibility.<sup>26</sup> A number of authors have proposed the use of modified implementations of FD<sup>27, 28</sup> as a textural descriptor in grey-level medical imaging to discriminate between tissue types, for instance.<sup>28, 29</sup> In dynamic PET imaging, fractal analysis has been used to characterize time activity curves.<sup>30</sup> However, to our knowledge no studies have investigated the  
80 potential of a fractal approach to recover space-filling properties of objects using PET imaging.

The main objective of this work was to use the FD estimate to recover the apparent space-filling index of a lesion (tumor volume, TV) embedded in non-zero background and subsequently use it to correct mean standardized uptake value ( $SUV_{\text{mean}}$ ) to obtain accurate total lesion activity (TLA) estimates from

85 approximate lesion contours. In other words, we aim to accurately recover the radioactive content of cancerous tissue via its geometrical properties estimated by fractal geometry.

The fractal, multifractal and space-filling factor concepts are introduced in the following section. The method is illustrated on mathematical objects, validated on realistic  $^{18}\text{F}$ -fluorodeoxyglucose ( $^{18}\text{F}$ -FDG) PET simulations and its face validity and reliability demonstrated on a test-retest  $^{18}\text{F}$ -fluorothymidine ( $^{18}\text{F}$ -FLT) PET clinical dataset.

## 2. THEORETICAL FRAMEWORK

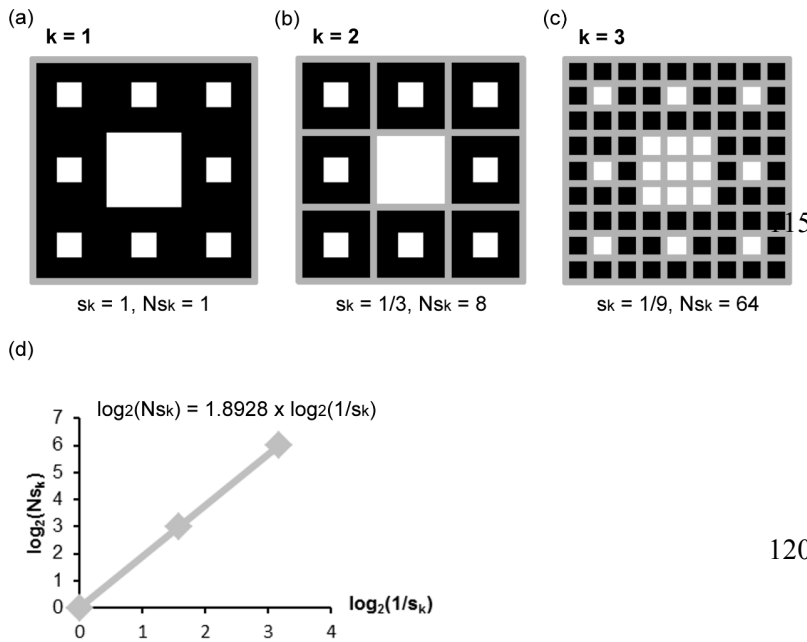
### 2.A. Fractal dimension

95 Fractal geometry and analysis were introduced by Mandelbrot<sup>15</sup> to describe mathematical and natural objects with highly irregular shapes. Many natural objects display the same amount of complexity at different scales.<sup>16</sup> When applied to these objects, classical measurements derived from Euclidian geometry (e.g. length, area or volume) become scale-dependent as new details are unravelled at higher resolutions.<sup>13, 15</sup> The fractal dimension (FD), which introduces a fractional component to dimension, has  
100 been proposed to capture the relationship between scale and measurement. Many definitions of FD have been proposed, including the one stemming from the box-counting method that is often preferred in practice.<sup>14, 31</sup> FD estimation using the box-counting method is illustrated on the Sierpinski carpet, a self-similar fractal object, in Fig.1. The box-counting method entails superimposing a grid of mesh size  $s_k$  onto the object of interest and in counting the number of boxes  $N_{s_k}$  of the grid that the object falls into  
105 (Fig.1(a)). The process is repeated for a number of coverings  $k$  with different mesh sizes  $s_k$  so as to count the number of boxes  $N_{s_k}$  needed to cover the object across scales. FD is defined as the power law

between  $N_{s_k}$  and the scale of measurement  $s_k$ , and can be obtained by fitting a regression line through the data points of the  $\log(N_{s_k})$  versus  $\log(1/s_k)$  plot as shown in Fig.1(b):

$$FD = \lim_{s_k \rightarrow 0} \frac{\log(N_{s_k})}{\log(1/s_k)} \quad (1)$$

110 with  $N_{s_k}$ : number of boxes occupied by the object and  $s_k$ : associated scale at the  $k^{\text{th}}$  covering. The box-counting method yields  $FD = 1.8928$  for the Sierpinski carpet.



125 FIG.1. Illustration of FD computation using the box-counting method on the Sierpinski carpet (2 iterations, 9x9 pixels image). (a) Image meshing using successive grids of different widths corresponding to  $s_k = 1, 1/3$  and  $1/9$  of the image length from left to right (covering index  $k = 1$  to 3), and (b) log-log plot (quantity  $N_{s_k}$  vs.  $1/s_k$ ) and fit of the regression line to obtain the fractal dimension.

## 2.B. A spectrum of FDs: the Generalized Rényi spectrum for non-uniform objects

A unifying multifractal framework has been proposed<sup>13, 14</sup> to compute FDs of objects characterized by non-uniform intensity distributions. Similar to the box-counting method for estimating a single-value FD, 130 the computation of the generalized Rényi FDs spectrum is based on the partitioning of a square-box image into sub-squares of identical sizes at different scales  $s_k$ . In the generalized approach, the quantity

## Willaime *et al*: Space-filling index and PET quantification

of interest at each scale  $s_k$  is not a binary measurement (number of boxes  $N_{s_k}$ ) but takes into account how much the object falls into each of the sub-squares (or *vel* – volume element) of the grid. The density of the object in the  $i^{\text{th}}$  *vel* at the  $k^{\text{th}}$  covering is defined as follows:

$$135 \quad p_{i,k} = \frac{I_{i,k}}{\sum_{i,k}^{N_{s_k}} I_{i,k}}, \quad (2)$$

where  $I_{i,k} = \sum_{v \in \text{vel}(i,k)} I(v)$ , that is, the intensity in the  $i^{\text{th}}$  *vel* at the  $k^{\text{th}}$  covering is the sum of the intensities of the voxels  $v$  belonging to the *vel*, and  $\sum_{i,k}^{N_{s_k}} I_{i,k}$  is the total mass (or intensity) in the square box. The measurement is normalized so that the sum of probabilities  $p_{i,k}$  equals unity at each  $k$  covering.

The Rényi FDs ( $D_q$ ) are obtained by weighting the probabilities  $p_{i,k}$  using a range of arbitrary moments  $q$ :

$$140 \quad D_q = \begin{cases} \lim_{s_k \rightarrow 0} \frac{1}{1-q} \frac{\log_2 \sum_{i=1}^{N_{s_k}} p_{i,k}^q}{\log_2(1/s_k)} & \text{for } q \neq 1 \\ \lim_{s_k \rightarrow 0} \frac{-\sum_{i=1}^{N_{s_k}} p_{i,k} \log_2 p_{i,k}}{\log_2(1/s_k)} & \text{for } q = 1 \end{cases} \quad (3)$$

The moment  $q$  emphasizes different intensity contributions in the image, with  $q = 0$  weighting all the radiotracer activity concentrations equally (i.e. box-counting FD),  $q = 1$  reducing to the information fractal dimension (rule of L'Hospital's). As  $q \rightarrow +\infty$  the Rényi entropy is determined by the contributions of the densest regions. For multifractal objects the moment  $q$  describes the entire spectrum of power-laws that defines the object. Examples of ( $D_q, q$ ) spectrums are given in Fig.2. The same total object intensity ( $\sum I_{\text{obj}}$ ) was spread in a uniform (Fig.2(a)) and in a non-uniform (Fig.2 (b)) fashion on the 64 pixels of a 9-  
150 pixel wide ( $L$ ) Sierpinski carpet.  $\sum I_{\text{obj}}$  was mostly concentrated within 16 voxels for the non-homogeneous Sierpinski carpet (Fig.2(b)), with other voxels of the object characterized by intensities only marginally greater than background. Although the box-counting dimension of these two objects is identical ( $D_0 = 1.8928$ ), the multifractal spectrum yields additional information about their intensity

distributions. Typically, the multifractal spectrum of a mono-fractal object is flat, whereas a non-  
 155 uniformly distributed object is characterized by an inverted S-shaped ( $D_q, q$ ) spectrum (Fig.2(c)).<sup>13</sup>

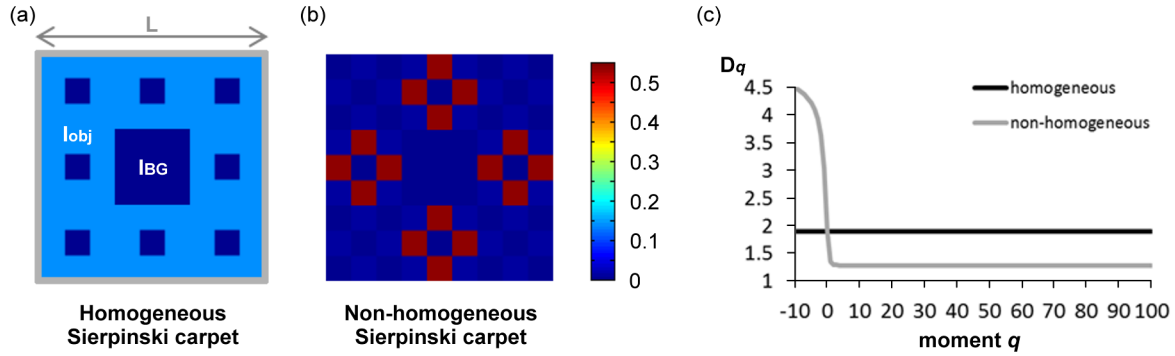


FIG.2. Illustration of (a) homogeneous and (b) non-homogeneous intensity distributions on a Sierpinski carpet, and (c) associated multifractal Rényi ( $D_q, q$ ) spectrums. The same total object intensity ( $\sum I_{obj} = 9$ ) was used in (a) and (b).  $L$  was the length of the square-box used for the Rényi FDs computation,  $I_{obj}$  and  $I_{BG}$  were the mean intensities in the object and in the background respectively.

160

### 2.C. From FD to a space-filling index

By definition of the fractal dimension (Eq. (1)), the area occupied by an object of interest can be recovered as follows:<sup>14, 18</sup>

$$\text{Area}_{FD} = c \times L^{FD} = L^{FD} \tag{4}$$

165 where  $L$  is the width of a square box positioned around the object and FD the fractal dimension that can be estimated using Eq. (1),  $\log_2(c)$  is the y-intercept of the log-log plot (Fig.1(b), with  $c$  equals 1). It follows that the area occupied by the 9-pixel wide Sierpinski carpet (Fig.2(a)) can be estimated as follows:  $\text{Area}_{FD} = 9^{1.8928} = 64$  pixels. Similarly, FD equals 2 for a unit cube of width 9x9 pixels (which is also the Euclidian dimension for a plane), and the number of pixels can be estimated as follows:  $\text{Area}_{FD} =$   
 170  $9^2 = 81$  pixels. Using the unified approach,<sup>13</sup> one can compute  $\text{Area}_{FD}(q)$  for each FD of the Rényi multifractal spectrum, characterizing the area occupied by different densities of an object of interest. Using the plateau of the ( $D_q, q$ ) spectrum (for greater  $q$ 's), one characterizes the most active area of the

## Willaime *et al*: Space-filling index and PET quantification

object. For instance, for the non-homogeneous Sierpinski carpet (Fig.2 (b)), one recovers  $FD = 1.2806$  (for  $FD = D_{q>10}$ ) and  $Area_{FD} = 9^{1.2806} = 16.7$  pixels.

175 For non-zero background, an estimate of mean background intensity ( $I_{BG}$ ) around the object of interest is computed and subtracted from the voxels' intensities in the square box of width  $L$ , prior to the Rényi FDs spectrum calculation. This ensures that the contributions of the background are minimized when estimating the  $Area_{FD}$ . Therefore, the “total mass”  $\sum_{i,k}^{N_{sk}} I_{i,k}$  in the square box used for the Rényi FD computation equals TLA for an object in zero background only.

### 180 **2.C.1. Correction of intensity descriptors: standardized uptake value ( $SUV_{FD}$ ) and total lesion activity ( $TLA_{FD}$ )**

Unlike traditional methods used to compute the area or the volume of a lesion, the computation of  $Area_{FD}$  does not require a defined contour for the lesion embedded in background.  $Area_{FD}$  can then be effectively used to correct the mean intensity measured in an approximate contour drawn around a lesion (containing 185 the object, PVE-contaminated voxels and some background voxels). Possible contours include the square box of width  $L$  used for  $Area_{FD}$  computation or, alternatively, a free-form rough contour. Corrected SUV (or  $I_{obj}$  in non-normalized images) and TLA (or  $\sum I_{obj}$ ) estimates can be recovered from 2D images as follows:

$$SUV_{FD} = \frac{1}{ff} \times SUV_{Contour} - \frac{(1-ff)}{ff} \times SUV_{BG} \quad (5)$$

$$190 \quad TLA_{FD} = Area_{Contour} \times SUV_{Contour} - (Area_{Contour} - Area_{FD}) \times SUV_{BG} \quad (6)$$

Where  $SUV_{Contour}$  and  $Area_{Contour}$  are  $SUV_{mean}$  and area estimates in the approximate contour,  $ff$  is the Filling-Factor computed as the ratio of  $Area_{FD}$  and  $Area_{contour}$ , and  $SUV_{BG}$  is an estimate of background intensity.  $ff$  represents the percentage of the square box occupied by the object (from 0 to 1) and reduces to  $L^{FD-2}$  for a square box.<sup>18</sup> Equation (5) yields  $I_{obj} = 0.14$  for the mono-fractal Sierpinski carpet (exactly equal to  $\sum I_{obj} / Area_{FD} = 9/64$ ) and  $I_{obj} = 0.54$  for the non-homogeneous case ( $\approx 9/16$ ). See supplemental 195

material (Suppl. Fig.1 and Suppl. Table I) at [URL] for examples of FD estimates for Sierpinski objects embedded in constant background ( $I_{BG} = 1$ ) and blurred at a resolution typical of PET imaging.

### 2.C.2. Volumetric features

200 The technique can be extended to 3D PET datasets by repeating the procedure on all slices of the image in which the object is visible. Volumetric descriptors ( $VOL_{FD}$ ,  $SUV_{FD}$  and  $TLA_{FD}$ ) can be obtained as follows:

$$VOL_{FD}(q) = \sum_{slice} Area_{FD}(q) \quad (7)$$

$$SUV_{FD}(q) = \frac{\sum_{slice}[Area_{FD}(q) \times SUV_{FD\ slice}(q)]}{\sum_{slice} Area_{FD}(q)} \quad (8)$$

205  $TLA_{FD}(q) = \sum_{slice} TLA_{FD\ in-slice}(q) \quad (9)$

This slice-by-slice stacked implementation was further compared to a full 3D approach (Suppl. Material., Section 7).

## 3. MATERIALS AND METHODS

### 210 3.A. Datasets

#### 3.A.1. Synthetic simulations

Synthetic simulations were generated to illustrate algorithm performance on homogeneous, rim-like and hot-spot-like uptake patterns (Fig.3 and Table I). Arbitrary contours were manually drawn in 32x32 pixel images using MATLAB version R2011a (The Mathworks, Natick, MA, USA). Lesions were attributed a  
215 range of target-to-background ratios (TBRs; 2:1, 4:1 and 6:1). White Gaussian noise ( $\mu = 0$ ,  $\sigma = 1$ ) was

added and the images were smoothed using a Gaussian filter (2- and 3-pixel full-width at half-maximum; FWHM).

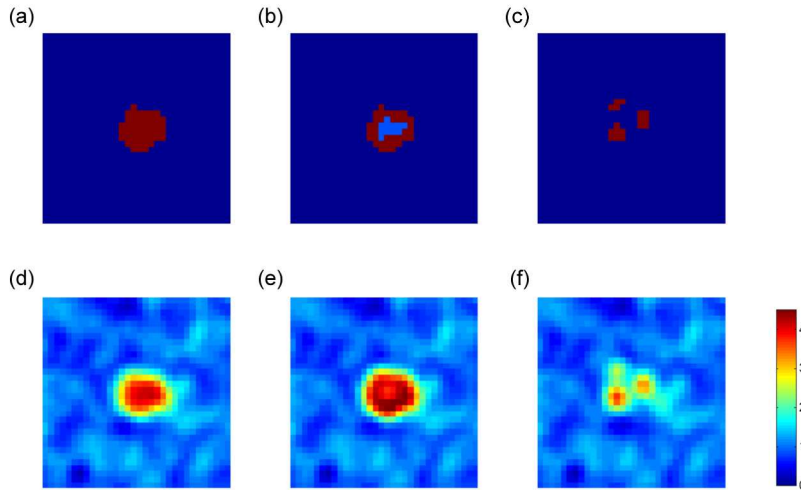


FIG.3. Examples of synthetic simulations: (a) homogeneous uptake pattern, (b) rim-core-like uptake pattern, and (c) hot-spot-like uptake pattern. Original images (no PVEs) and examples of corresponding noisy images (3-voxel FWHM Gaussian post-filtered) are displayed on the top and bottom rows respectively.

230

TABLE I. Ground truth (GT) for synthetic simulations: lesion size ( $Area_{GT}$ ), mean uptake value ( $SUV_{GT}$ ) and total lesion activity ( $TLA_{GT}$ ).

Uptake pattern	Case	$Area_{GT}$	$SUV_{GT}$	$TLA_{GT}$
Homogeneous	1	46 pixels	6	276
	2		4	184
	3		2	92
Rim-core-like	4	Rim = 35 pixels Core = 11 pixels	Rim: 6 Core: 4	254
	5		Rim: 6 Core: 2	232
	6		Rim: 6 Core: 1	210
Hot-spot-like	7	Hot-spot 1 = 4 pixels Hot-spot 2 = 6 pixels Hot-spot 3 = 7 pixels	All Hot-spots: 6	102
	8		Hot-spot 1: 6 Hot-spot 2: 4 Hot-spot 3: 2	62

235

### 3.A.2. Realistic $^{18}\text{F}$ -FDG PET simulations

Ground truth assessment of the method was performed using published realistic PET simulations.<sup>32</sup> The fast analytic simulation toolkit employed to generate the datasets has been described elsewhere.<sup>33, 34</sup> Briefly, PET images were generated using dynamic real MR images, incorporating motion information, and typical physiological uptake values of  $^{18}\text{F}$ -FDG in thorax, normalized for body weight ( $\text{SUV}_{\text{BW}}$ ). Spherical lesions of different size and filled-in with uniformly distributed radiotracer uptakes were inserted into lung and liver (Table II). Corresponding PET sinograms were simulated for a PET Gemini TF Scanner such that they followed a Poisson distribution as discussed by Tsoumpas et al.<sup>33</sup> Data were reconstructed using STIR software<sup>35</sup> and the OSEM algorithm (23 subsets) for a range of iterations (1, 2, 3, 5, 10, 15 and 20). Image size was  $250 \times 250 \times 87$  voxels and voxel size was set to  $2 \times 2 \times 2 \text{ mm}^3$ . Images were reconstructed with and without motion-compensated image reconstruction (MCIR) and post-filtered (4 and 5 mm Gaussian smoothing).

TABLE II. Ground truth for realistic PET simulations:  $\text{SUV}_{\text{BG}}$  ( $\text{SUV}_{\text{mean}}$  in background tissue), lesion size ( $\text{VOL}_{\text{GT}}$ ,  $\text{cm}^3$ ),  $\text{SUV}_{\text{GT}}$  ( $\text{SUV}_{\text{mean}}$  in lesion),  $\text{TLA}_{\text{GT}}$  and Standardized Added Metabolic activity (SAM).

Lesion	Location	$\text{SUV}_{\text{BG}}$ (g/mL)	$\text{VOL}_{\text{GT}}$ ( $\text{cm}^3$ )	$\text{SUV}_{\text{GT}}$ (g/mL)	$\text{TLA}_{\text{GT}}$ (g)	$\text{SAM}_{\text{GT}}$ (g)
1	Lung	0.50	0.52	4.5	2.36	2.10
2	Lung	0.50	2.14	4.5	9.65	8.58
3	Lung	0.50	2.14	7.5	16.08	15.01
4	Liver	2.50	0.52	6.5	3.40	2.10
5	Liver	2.50	2.14	6.5	13.94	8.59
6	Liver	2.50	2.14	9.5	20.37	15.02

250

### 3.A.3. Test-retest $^{18}\text{F}$ -FLT PET clinical dataset

An  $^{18}\text{F}$ -FLT PET breast cancer dataset was used to assess the repeatability of the method<sup>36-38</sup> in patients who underwent a baseline and a validation scan, within 2 to 8 days, prior to treatment. Dataset included 6 primary lesions, 1 lung and 1 rib metastasis, 1 axillary and 1 pre-tracheal node in a total of 8 patients.

255

### **Willaime *et al*: Space-filling index and PET quantification**

PET images were acquired dynamically for 95 minutes using an ECAT 962/HR+ scanner (CTI/Siemens, Knoxville, TN, USA). Analyses were performed on post-filtered iteratively reconstructed PET images (OSEM, 5mm FWHM Gaussian Filter) on one time frame (at 60 minutes, 10 minutes duration). The variability in FD within individual tumors was estimated by computing relative differences ( $\Delta$ ) between baseline and validation scans:  $(\text{feat}_{\text{baseline}} - \text{feat}_{\text{validation}}) / [(\text{feat}_{\text{baseline}} + \text{feat}_{\text{validation}}) / 2]$ . Bland-Altman analysis was performed and 95% upper and lower repeatability limits (URL and LRL, respectively) computed as mean  $\pm$  1.96xSD of the relative differences. The intraclass correlation coefficient (ICC) was also calculated to assess the repeatability of the image descriptor measurements for the group of patients included in this study, as previously described.<sup>38</sup> All the slices in which the lesion was visible were included in the analysis.

### **3.B. Influence of partial volume correction (PVC)**

We studied the impact of PVEs and PVC on FD estimates using the Lucy-Richardson iterative deconvolution methodology,<sup>39, 40</sup> with incorporated wavelet denoising using Bayeshrink filtering.<sup>41</sup> The PVC technique assumed a spatially invariant point spread function (PSF) for the scanner and was implemented in C++ (in-house software, Imperial College London, London, UK). For comparison, a PSF of both 4.3mm and 5mm were used. The analyses were performed on the realistic <sup>18</sup>F-FDG PET simulations (MCIR, 15 iterations and 5mm post-filtering).

### **3.C. Filling-Factor software (FFS) and statistical analyses**

The multifractal methodology was implemented in MATLAB, as a toolbox and graphical user interface, Filling-Factor Software (FFS). All computations were performed using FFS. The Rényi multifractal spectrum was estimated using multiple grid sizes and positions around the object of interest, so as to

## Willaime *et al*: Space-filling index and PET quantification

study the influence on space-filling estimates. The corresponding square boxes were also used as  
280 approximate lesion contours to measure  $SUV_{\text{contour}}$  and  $TLA_{\text{contour}}$  prior to intensity estimates correction.  
Structures different from background and object were manually segmented and excluded from the  
analyses. FD estimates were obtained using the linear least squares method and a minimum of three  
scales. FD estimates were reported for one moment  $q$  of the plateau in tables ( $q = 50$ ). Variations in FD  
estimates across moments of the plateau ( $30 \leq q \leq 100$ ) were also given in the main text.

285 All statistical analyses were performed using SPSS for Windows version 21 (IBM, Chicago, IL, USA).

### 3.D. Comparative methods

We compared the performance of the present methodology to the Standardized Added Metabolic activity  
(SAM)<sup>42</sup>, a recently proposed metric for <sup>18</sup>F-FDG PET. By definition the information provided by SAM  
290 is different from TLA. However, both require similar user inputs. SAM is computed by drawing a first  
VOI around the lesion (VOI1) and a second VOI in the background surrounding the object (VOI2). The  
mean background intensity ( $I_{\text{BG}}$ ) is computed using all voxels in VOI2 that do not belong to VOI1. The  
index is obtained as total intensity VOI1 – ( $I_{\text{BG}}$  x volume VOI1). SAM was applied to the realistic <sup>18</sup>F-  
FDG PET simulations (MCIR, 15 iterations and 5mm post-filtering) with and without PVE correction.

295

## 4. RESULTS

### 4.A. Space-filling and intensity recovery for different uptake patterns, TBR and image resolutions

300 We tested the method on different uptake patterns: homogeneous, rim-core-like and hot-spot-like, for a  
range of TBRs (Fig.3). Results of the analyses ( $Area_{\text{FD}}$ ,  $SUV_{\text{FD}}$  and  $TLA_{\text{FD}}$ ) were compared to ground  
truth (Table III). The dependency of  $Area_{\text{FD}}$  and  $SUV_{\text{FD}}$  on image resolution was observed in all cases (2

## Willaime *et al*: Space-filling index and PET quantification

versus 3-voxel FWHM Gaussian smoothing). The magnitude with which image resolution affected  $\text{Area}_{\text{FD}}$  and  $\text{SUV}_{\text{FD}}$  estimates depended on the object (shape and size) as well as on TBR. VOI size  
305 underestimation was less than -17% in all cases, except for the lowest TBR (2:1) for the homogeneous uptake pattern (-31%, case 3). Object size overestimation (due to smoothing), was object dependent: up to +15% in the case of rim-core-like uptake patterns with a core intensity different from the background intensity, up to +50.5% in the case of a rim-core-like uptake pattern with a core intensity identical to background, and up to +82% in the case of a hot-spot-like pattern.  $\text{TlA}_{\text{GT}}$  was recovered within a few  
310 percent error ( $\pm 13\%$ ) in all cases. Additional simulations showed that the large  $\text{Area}_{\text{FD}}$  overestimation for the hot-spot-like pattern was due to object size (Suppl. Fig.2 and 3). The coefficients of determination  $R^2$  of the regression line for FD estimation were very high (mean = 0.95, standard deviation = 0.02). 96.6% of all computations (N = 408) yielded  $R^2 > 0.9$ . The variation in FD estimates, measured using the coefficient of variation, across moment  $q$  between 30 and 100 (for the plateau) was negligible across all  
315 computations (mean  $\pm$  standard deviation;  $D_q$ :  $0.42\% \pm 0.20\%$ ;  $\text{Area}_{\text{FD}}(q)$ :  $1.43\% \pm 0.67\%$ ;  $\text{TlA}_{\text{FD}}(q) = 0.31\% \pm 0.22\%$ ;  $\text{I}_{\text{FD}}(q) = 1.10\% \pm 0.53\%$ ). Further, the impact of background heterogeneity was illustrated with an object of interest located at the interface between two background regions of low and high intensities. The mean background intensity was estimated by dilatation of the approximate contour drawn around the object of interest (Suppl. Fig. 4). Providing an accurate estimation of the mean  
320 background intensity surrounding the object of interest, TLA was recovered within less than 12% error (Suppl. Table II).

325 TABLE III. FD estimates (mean and standard-deviation across box sizes and positions, and percent error) for synthetic simulations.

Uptake pattern	Case	Smoothing	Area <sub>FD</sub> (voxels)	SUV <sub>FD</sub>	TLA <sub>FD</sub>
Homogeneous	1	2 voxels	40.2 ± 4.0 (-12.6%)	7.1 ± 0.6 (14.2%)	281.2 ± 4.8 (-1.1%)
		3 voxels	43.8 ± 4.1 (-4.8%)	6.6 ± 0.5 (6.3%)	285.4 ± 4.6 (0.4%)
	2	2 voxels	38.3 ± 3.5 (-16.8%)	4.9 ± 0.4 (17.9%)	187.3 ± 4.5 (-2.6%)
		3 voxels	44.3 ± 3.7 (-3.6%)	4.4 ± 0.3 (5.8%)	194.8 ± 4.4 (1.4%)
	3	2 voxels	31.6 ± 2.6 (-31.4%)	2.8 ± 0.2 (29.1%)	88.5 ± 5.8 (-11.7%)
		3 voxels	43.3 ± 3.2 (-5.9%)	2.4 ± 0.1 (9.1%)	102.7 ± 5.9 (2.5%)
Rim-core-like	4	2 voxels	42.0 ± 3.9 (-8.6%)	6.3 ± 0.5 (9.8%)	261.1 ± 4.8 (-0.4%)
		3 voxels	49.4 ± 4.2 (7.3%)	5.5 ± 0.4 (-3.8%)	269.1 ± 4.7 (2.6%)
	5	2 voxels	40.9 ± 3.6 (-11.2%)	5.9 ± 0.4 (12.2%)	237.9 ± 4.5 (-1.0%)
		3 voxels	52.7 ± 4.3 (14.6%)	4.8 ± 0.3 (-8.5%)	250.6 ± 4.8 (4.3%)
	6	2 voxels	39.0 ± 3.3 (11.4%)	5.8 ± 0.4 (-7.1%)	225.0 ± 4.4 (2.9%)
		3 voxels	52.7 ± 4.0 (50.5%)	4.6 ± 0.3 (-26.8%)	239.7 ± 4.7 (9.6%)
Hot-spot-like	7	2 voxels	18.8 ± 2.5 (10.5%)	5.4 ± 0.4 (-13.5%)	101.1 ± 8.2 (-5.3%)
		3 voxels	30.1 ± 3.0 (77.2%)	3.7 ± 0.2 (-40.6%)	111.9 ± 7.3 (4.8%)
	8	2 voxels	16.1 ± 3.1 (-5.5%)	3.7 ± 0.2 (-6.7%)	58.4 ± 9.1 (-12.6%)
		3 voxels	30.9 ± 4.7 (81.7%)	2.4 ± 0.1 (-39.5%)	73.1 ± 9.7 (9.4%)

#### 4.B. Recovery of TLA as a function of reconstruction parameters

330 A plateau was reached after 5 to 10 iterations (115-230 updates) for all realistic PET datasets yielding stable results in the recovery of TLA estimates. See supplemental material (Suppl. Fig.5) for results of the recovery of TLA estimates on reconstructed PET images after varying number of iterations. The percent error was less than ±15% for all lesions on images post-filtered and motion-corrected. PET images not corrected for motion (NMC) yielded larger errors in the estimates recovered. The coefficients of determination  $R^2$  of the regression line for FD estimation were very high (mean = 0.95, standard deviation = 0.07). 91.2% of all computations (N = 22,139) yielded  $R^2 > 0.9$ . The variation in FD estimates across moment  $q$  between 30 and 100 was negligible ( $D_q$ : 0.52% ± 0.12%;  $VOL_{FD}(q)$ : 1.82% ± 0.29%;  $TLA_{FD}(q)$  = 0.57% ± 0.34%;  $SUV_{FD}(q)$  = 1.21% ± 0.24%), across all computations.

**4.C. Effects of PVC on FD estimates**

Applying PVC by specifying successively larger scanner PSF (4.3mm and 5mm) led to an increasingly concentrated radiotracer uptake in space. See supplemental material (Suppl. Fig.6) for an example of a realistic PET image corrected for PVEs. These visual observations were confirmed by the feature value recovered for  $VOL_{FD}$  and  $SUV_{FD}$  (Table IV) across image resolutions (no PVC, 4.3mm PSF and 5mm PSF), with a consistent decrease in  $VOL_{FD}$  (and increase in  $SUV_{FD}$ ) for increasing PSF specified. Percent error in  $VOL_{FD}$  decreased with PVC for all lesions, but remained up to +36%. Reasonably stable values of  $TLA_{FD}$  were obtained for all lesions across the different image resolutions. The ground truth TLA was recovered within  $\pm 13\%$  in all cases. SAM was recovered within  $\pm 17.5\%$  across all datasets (Table V), and displayed a similar degree of variability as TLA across image resolutions.

TABLE IV. Impact of image resolution (PVC) on mean FD estimates (and percent error). Images were reconstructed with OSEM using 15 iterations, motion-corrected (MCIR) and post-filtered (5mm FWHM Gaussian Filter).

Lesion	$VOL_{FD} (cm^3)$			$SUV_{FD} (g/mL)$			$TLA_{FD} (g)$		
	No PVC	4.3 mm PSF	5mm PSF	No PVC	4.3 mm PSF	5mm PSF	No PVC	4.3 mm PSF	5mm PSF
1	0.98 (+87.6%)	0.77 (+49.6%)	0.71 (+36%)	2.18 (-51.7%)	2.67 (-40.7%)	2.90 (-35.6%)	2.12 (-10.1%)	2.08 (-12%)	2.05 (-13.1%)
2	3.14 (+46.6%)	2.83 (+32.4%)	2.68 (+25.2%)	3.36 (-25.3%)	3.71 (-17.6%)	3.89 (-13.7%)	10.54 (+9.2%)	10.51 (+8.9%)	10.41 (+7.9%)
3	3.37 (+57.6%)	3.00 (+40.1%)	2.81 (+31.4%)	4.97 (-33.8%)	5.58 (-25.6%)	5.91 (-21.2%)	16.75 (+4.2%)	16.74 (+4.1%)	16.62 (+3.4%)
4	0.89 (+70.0%)	0.70 (+34.1%)	0.64 (+23.7%)	4.30 (-33.8%)	4.99 (-23.2%)	5.30 (-18.4%)	3.80 (+11.9%)	3.48 (+2.4%)	3.41 (+0.32%)
5	2.68 (+25.3%)	2.29 (+6.9%)	2.13 (-0.2%)	5.51 (-15.3%)	6.11 (-6.0%)	6.41 (-1.4%)	14.77 (+5.9%)	13.99 (+0.3%)	13.69 (-1.8%)
6	2.68 (+25.1%)	2.35 (+9.8%)	2.23 (+4.0%)	7.13 (-24.9%)	7.94 (-16.5%)	8.29 (-12.7%)	19.09 (-6.26%)	18.65 (-8.4%)	18.46 (-9.4%)

355 TABLE V. SAM values (and percent error) for different image resolutions. Images were reconstructed with OSEM using 15 iterations, motion-corrected (MCIR) and post-filtered (5mm FWHM Gaussian Filter).

Lesion	SAM (g)		
	No PVC	4.3 mm PSF	5mm PSF
1	1.76 (-16.2%)	1.81 (-13.7%)	1.83 (-13.1%)
2	8.50 (-0.9%)	8.70 (+1.4%)	8.72 (+1.6%)
3	14.61 (-2.67%)	14.82 (-1.2%)	14.83 (-1.2%)
4	1.75 (-16.51%)	1.91 (-9.2%)	1.97 (-6.0%)
5	7.90 (-8.08%)	8.09 (-5.8%)	8.17 (-4.9%)
6	12.39 (-17.51%)	12.84 (-14.5%)	12.98 (-13.6%)

360 **4.D. Clinical validation: robustness of the approach**

FD estimates ( $VOL_{FD}$ ,  $SUV_{FD}$  and  $TLA_{FD}$ ) for individual lesions and scans, as well as relative differences between baseline and validation scans, are given in Suppl. Table III. All volumes were recovered within a variability of approximately  $\pm 15\%$ , except for patient 7 (+ 33%), for whom the tumor volume was hardly visible in the second scan. Repeatability results (relative differences and ICC coefficients) for the three estimates ( $VOL_{FD}$ ,  $SUV_{FD}$  and  $TLA_{FD}$ ) are given in Table VI. The results are presented both including and excluding patient 7 for whom large variations in SUV uptake were observed both with the FD method (+44%, Suppl. Table III) and using the original mask delineated by the clinician (+50%). This variability at baseline might be due to either some biological change that happened in this lesion between the two successive scans, and/or to a problem of detectability. ICC results are presented excluding the primary lesion of patient 4 for  $TLA_{FD}$  and  $VOL_{FD}$  as the lesion was very large in comparison to other primary tumors. When excluding patient 7, the variability across all lesions (mean  $\pm$  standard deviation) was  $1.8\% \pm 8.5\%$  for  $VOL_{FD}$ ,  $4.6\% \pm 13.2\%$  for  $SUV_{FD}$  and  $10.3\% \pm 12.2\%$  for  $TLA_{FD}$  (Table VI). Relative differences between baseline and validation scans were not statistically different from a normal

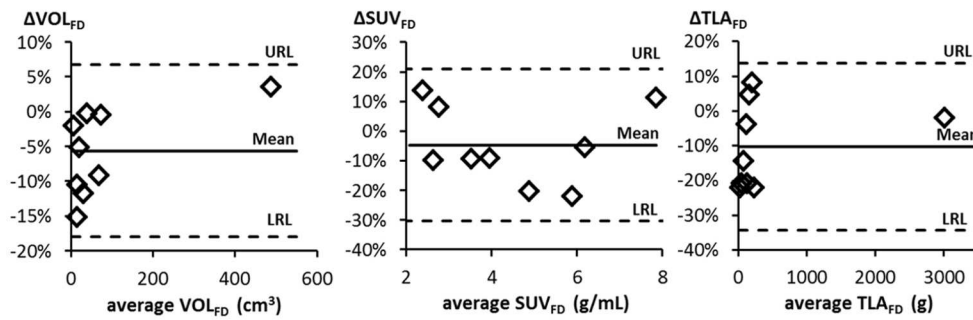
**Willaime *et al*: Space-filling index and PET quantification**

distribution (Shapiro-Wilk test,  $p > 0.05$ ). When excluding patient 7, URL and LRL across all lesions were  
 375 -18% to 7% for  $VOL_{FD}$ , -30% to 20% for  $SUV_{FD}$  and -30% to 37.4% for  $TLA_{FD}$  (Fig. 4). The coefficients  
 of determination  $R^2$  of the regression line for FD estimation were very high (mean = 0.98, standard  
 deviation = 0.03). 98.3% of all computations ( $N = 21,325$ ) yielded  $R^2 > 0.9$ .

380 TABLE VI. Repeatability results for  $^{18}F$ -FLT PET dataset. % variations were computed from relative  
 differences ( $\Delta$  mean  $\pm$  standard-deviation across lesions)

Analysis	Lesion	$VOL_{FD}$ (cm <sup>3</sup> )		$SUV_{FD}$ (g/mL)		$TLA_{FD}$ (g)	
		% variation	ICC	% variation	ICC	% variation	ICC
with patient 7	All	4.9 $\pm$ 12.7	0.99*	8.6 $\pm$ 17.6	0.94	16.7 $\pm$ 23.4	0.96*
	primary only	9.3 $\pm$ 12.9	0.99*	7.6 $\pm$ 20.4	0.95	16.4 $\pm$ 30.5	0.98*
without patient 7	All	1.8 $\pm$ 8.5	0.99*	4.6 $\pm$ 13.2	0.94	10.3 $\pm$ 12.2	0.96*
	primary only	4.6 $\pm$ 6.3	0.99*	0.2 $\pm$ 10.8	0.98	4.8 $\pm$ 12.4	0.96*

\* without patient 4



385 FIG.4. Bland-Altman plots of FD estimates. Lines show mean, upper and lower limits of repeatability (URL, LRL). All patients except patient 7 were included.

The slice-by slice stacked implementation proposed was further compared to a full 3D implementation. The latter yielded no improvements on synthetic and realistic PET simulations (Suppl. Table IV).

## 5. DISCUSSION

390 In this work we have proposed an original method, based on a multifractal approach, for recovering the  
apparent space-filling properties of objects of interest from low resolution (PET) imaging. Results show  
that the method can be used to recover volume and intensity estimates of the active part(s) of a neoplastic  
lesion without any requirement for PVC. The technique was applied to a range of independent datasets  
including noisy synthetic simulations, realistic PET simulations and a clinical  $^{18}\text{F}$ -FLT PET dataset. For  
395 images with a resolution comparable to post-filtered PET images, TLA was generally recovered within  
15% error.

The proposed implementations only required limited user input and did not rely on a robust delineation of  
the lesion's voxels as in traditional frameworks. This could be an advantage as robust automatic  
400 segmentation tools are generally needed to derive TLA but are yet not systematically implemented.<sup>43</sup> TLA  
derived from the FD method, as a molecular-biochemical or metabolic measurement variable, might also  
provide more information to clinicians than simplified metrics such as SAM,<sup>42</sup> which corresponds to the  
excess radiotracer uptake in normal tissue in the presence of a lesion. TLA and SAM displayed similar  
degrees of variability across image resolutions (for different PVE corrections). However, by definition  
405 SAM is not equivalent to TLA, and it depends on the surrounding background intensity. The FD method  
is fundamentally different in that it provides an estimate of the area occupied by the lesion in order to  
correct estimates (such as TLA) obtained from similar generic inputs. The influence of object size on the  
recovery of FD estimates was exemplified by the higher over-estimation of the area for "hot-spot-like"  
than for "rim-core-like" cases. Firstly, "hot-spot-like" objects were at most half the size of the "rim-core-  
410 like" objects and therefore much more affected by PVEs. Secondly, the apparent area/volume observed in  
PET and estimated using the FD method depends on image resolution and PVEs as demonstrated on the  
different datasets. In contrast with traditional delineation methods that yield a binary classification of

## Willaime *et al*: Space-filling index and PET quantification

voxels<sup>44</sup> (e.g. lesion or background), the FD method takes into account all the voxels that contain some lesion activity during quantification. The approach might not be suitable for recovering the volume of the underlying lesion, but provides some potential advantages for quantification of the molecular processes being imaged. One of the main strengths of the FD method is the stability of TLA estimates at different image resolutions as demonstrated on simulated and clinical PET datasets. The results presented demonstrate that using the plateau of the  $(D_q, q)$  Rényi FDs spectrum is a sufficiently good approximation for estimating TLA in PET oncology. The moment  $q$  provides an automatic threshold, relatively straightforward to implement, internal to the FD method. However, the output of this multi-scale approach is not a contour or a binary image but a fractal dimension used to recover an area/volume estimate.

The computation of the space-filling index, corrected TLA and SUV estimates was fast. For example, it took approximately 5 seconds on an Intel Core I7 processor to compute results for one slice and 24 square boxes positioned around the object ( $L$  ranging from 14 to 20 pixels). The influence of moment  $q$  of the plateau used on the estimates was negligible (less than 2%). Mean indices (across grid sizes and positions) provided robust estimates and might be preferred to reduce the variability of results due to user input. Potential limitations of the method include errors in mean background estimate, which could propagate when correcting SUV and TLA values using Eq. 5 and 6. However, we found that minimizing potential errors by selecting the background appropriately (around the object, on multiple slices) as well as drawing regions of reasonable size around the object (containing mostly the object's voxels and a small number of the background's voxels) yielded reasonable results. The latter was easily implemented using the practical slice-by-slice stacked computation proposed in this paper, in contrast with a full 3D implementation which did not yield improved results (see section 7, Suppl. Material).

Performance depended on TBR, object size, shape and noise level as described in the literature using other segmentation and quantification approaches.<sup>45</sup> On synthetic simulations, FD estimates were

## Willaime *et al*: Space-filling index and PET quantification

recovered with greater accuracy for higher TBR, while lower TBR and noise led to underestimation of space-filling index and TLA in some cases.

440 There are limitations to this methodology. Firstly, given the limited resolution in PET, the number of scales used for the FD estimations was bound by the voxel width and by the object width (approximately). The box size was kept relatively similar to the object so as to maintain a significant proportion of object voxels vs. background voxels. A minimum of three scales was used with all possible meshes between these bounds so as to maximize the number of points used for FD estimations. No  
445 interpolation was employed in the present work. The values obtained for the coefficients of determination of the regression line for FD estimation were very high in all datasets ( $R^2 \geq 0.95$  on average and  $R^2 > 0.9$  in more than 90% of all computations), confirming that the method is of great applicability in this context. Natural and biological objects often differ from mathematical fractals in that they are not self-similar across scales. The range of scales at which these natural entities can be investigated is also finite (i.e.  
450 bound by the resolution of an imaging system and the size of the object of interest).<sup>46</sup> Nevertheless, in the same way one uses ideal shapes derived from Euclidian geometry to characterize an object, one can use fractal analysis to characterize the complexity and irregularities of biological entities.<sup>47</sup> FD might be more informative than smoothed measurements derived from Euclidian geometry when it comes to capturing the complexity of neoplastic lesions.<sup>47</sup> In this work, estimates were compared to ground truth and to the  
455 SAM methodology. The results for the repeatability study were similar to previously reported results using a fuzzy locally adaptive Bayesian (FLAB)<sup>48</sup> delineation algorithm (URL and LRL around  $\pm 30\%$  for TV,  $SUV_{\text{mean}}$  and TLA) on the same  $^{18}\text{F}$ -FLT PET dataset<sup>49</sup>. It would be of interest to study how the results compare to those obtained from robust automatic segmentation methods, such as fuzzy C-means and FLAB,<sup>48</sup> at different image resolutions. On realistic simulations, TLA was recovered within 15% on  
460 motion corrected images with the FD method, whereas the errors were quite large when using non-motion corrected images (up to 40%). As a consequence, although the FD method yielded good results in terms of repeatability (all volumes were recovered within  $\pm 15\%$ , except for one patient) it is likely that the

## **Willaime *et al*: Space-filling index and PET quantification**

corrected TLA values contained other sources of bias that could not be accounted for in this study. In the present work, PVC correction using the Lucy-Richardson algorithm was solely used to study the influence of image resolution on FD estimates; which may not necessarily be the best approach for PVC. Direct comparisons of the FD method to traditional workflows might depend on both the segmentation and PVC techniques employed. The work presented was focused on the theoretical development and practical validation of this novel methodology. It was beyond the scope of this first investigation to fully automate the technique, in particular with regard to user inputs. However, the current framework could be supplemented by existing methodologies to further automate the process and implement it for use in clinical practice.

The present framework could be extended to a range of other applications using functional and molecular imaging. This methodology provides an alternative to traditional Euclidian-based contouring methods for volume estimation. The space-filling index could be further combined with anatomical volumetric information (e.g. from CT or MR) to recover SUVs of PVE-contaminated structures using reliable  $TLA_{FD}$  estimates.

## **6. CONCLUSION**

A new image-based methodology was proposed for recovering the apparent volume and intensity space-filling properties of an object of interest in PET without a robust segmentation step. Without implying any clinical advantage in predicting outcome, results suggested that the method performs reasonably well in recovering TLA on post-filtered PET images. The accuracy and performance of the method needs to be assessed, in the clinical context, against existing workflows which incorporate image pre-processing steps (i.e. PVC and automatic segmentation) prior to quantification.

## ACKNOWLEDGEMENTS

The authors would like to thank Miss Irene Polycarpou for the realistic PET simulation dataset, as well as Dr. Laura Kenny and Dr. Amarnath Challapalli for their clinical input. The study was supported by  
490 Cancer Research UK and Engineering and Physical Sciences Research Council, in association with the MRC and Department of Health (England) Centre Grant C2536/A10337 and the UK Medical Research Council Programmatic funding (Oncology and PET Methodology Programs). Prof. Federico Turkheimer is supported by the MRC PET Methodology Programme Grant (G1100809/1).

## 495 CONFLICT OF INTEREST

Dr. Julien Willaime carried out this research as part of his Ph.D. at the Comprehensive Cancer Imaging Centre (Imperial College London, London, UK). He is now an employee of Siemens.

<sup>a)</sup> Author to whom correspondence should be addressed. Electronic mail: [julien.willaime@siemens.com](mailto:julien.willaime@siemens.com)

- 500 <sup>1</sup> B. Bai, J. Bading, and P.S. Conti, "Tumor quantification in clinical positron emission tomography," *Theranostics* **3**, 787-801 (2013).
- <sup>2</sup> R. Boellaard, "Standards for PET image acquisition and quantitative data analysis," *J. Nucl. Med.* **50** Suppl **1**, 11S-20S (2009).
- 505 <sup>3</sup> O. Rousset, A. Rahmim, A. Alavi, and H. Zaidi, "Partial Volume Correction Strategies in PET," *PET Clinics* **2**, 235-249 (2007).
- <sup>4</sup> K. Erlandsson, I. Buvat, P.H. Pretorius, B.A. Thomas, and B.F. Hutton, "A review of partial volume correction techniques for emission tomography and their applications in neurology, cardiology and oncology," *Phys. Med. Biol.* **57**, R119-159 (2012).
- 510 <sup>5</sup> M. Soret, S.L. Bacharach, and I. Buvat, "Partial-volume effect in PET tumor imaging," *J. Nucl. Med.* **48**, 932-945 (2007).
- <sup>6</sup> R.L. Wahl, H. Jacene, Y. Kasamon, and M.A. Lodge, "From RECIST to PERCIST: Evolving Considerations for PET Response Criteria in Solid Tumors," *J. Nucl. Med.* **50**, 122S-150S (2009).
- <sup>7</sup> S.M. Larson, Y. Erdi, T. Akhurst, M. Mazumdar, H.A. Macapinlac, R.D. Finn, C. Casilla, M. Fazzari, N. Srivastava, H.W. Yeung, J.L. Humm, J. Guillem, R. Downey, M. Karpeh, A.E. Cohen, and R. Ginsberg, "Tumor Treatment Response Based on Visual and Quantitative Changes in Global Tumor Glycolysis Using PET-FDG Imaging. The Visual Response Score and the Change in Total Lesion Glycolysis," *Clin. Positron Imaging* **2**, 159-171 (1999).
- 515 <sup>8</sup> M. Hatt, D. Visvikis, O. Pradier, and C. Cheze-le Rest, "Baseline <sup>18</sup>F-FDG PET image-derived parameters for therapy response prediction in oesophageal cancer," *Eur. J. Nucl. Med. Mol. Imaging* **38**, 1595-1606 (2011).
- 520 <sup>9</sup> M. Hatt, C.C.L. Rest, A. Dekker, D. De Ruysscher, M. Oellers, P. Lambin, C. Roux, and D. Visvikis, "A new automatic methodology for functional volumes determination in emission imaging for oncology applications," *Irbm* **30**, 144-149 (2009).

## Willaime *et al*: Space-filling index and PET quantification

- 10 T. Shepherd, M. Teras, R.R. Beichel, R. Boellaard, M. Bruynooghe, V. Dicken, M.J. Gooding, P.J. Julyan, J.A. Lee, and S. Lefevre, "Comparative study with new accuracy metrics for target volume contouring in PET image guided radiation therapy," *IEEE Trans. Med. Imaging* **31**, 2006-2024 (2012).
- 525 11 M. Hatt, A. Le Pogam, D. Visvikis, O. Pradier, and C. Cheze Le Rest, "Impact of partial-volume effect correction on the predictive and prognostic value of baseline 18F-FDG PET images in esophageal cancer," *J. Nucl. Med.* **53**, 12-20 (2012).
- 12 B.B. Mandelbrot, "Multifractal measures, especially for the geophysicist," *Pageoph* **131**, 5-42 (1989).
- 530 13 W. Kinsner, "A unified approach to fractal dimensions," in *Fourth International Conference on Cognitive Informatics (IEEE)*, 2005, pp. 58-72.
- 14 H.-O. Peitgen, H. Jürgens, and D. Saupe, *Chaos and Fractals: New Frontier of Science*, 2nd Edition ed. (Springer, New-York, 2004).
- 15 B.B. Mandelbrot, *The fractal geometry of nature*. (Freeman, Oxford, 1982).
- 535 16 S.S. Cross, "Fractals in pathology," *J. Pathol.* **182**, 1-8 (1997).
- 17 A. Di Ieva, F. Grizzi, C. Sherif, C. Matula, and M. Tschabitscher, "Angioarchitectural heterogeneity in human glioblastoma multiforme: a fractal-based histopathological assessment," *Microvasc. Res.* **81**, 222-230 (2011).
- 18 M.J. Aschwanden and P.D. Aschwanden, "Solar Flare Geometries. I. The Area Fractal Dimension," *The Astrophys. J.* **674**, 530 (2008).
- 540 19 L. Norton, "Conceptual and Practical Implications of Breast Tissue Geometry: Toward a More Effective, Less Toxic Therapy," *The oncologist* **10**, 370-381 (2005).
- 20 D. Charalampidis, M. Pascotto, E.K. Kerut, and J.R. Lindner, "Anatomy and flow in normal and ischemic microvasculature based on a novel temporal fractal dimension analysis algorithm using contrast enhanced ultrasound," *IEEE Trans. Med. Imaging* **25**, 1079-1086 (2006).
- 545 21 M. Kleen, O. Habler, B. Zwissler, and K. Messmer, "Programs for assessment of spatial heterogeneity of regional organ blood flow," *Comput. Methods Programs Biomed.* **55**, 51-57 (1998).
- 22 S.H. Carbonetto and S.E. Lew, "Characterization of border structure using fractal dimension in melanomas," *Conf. Proc. IEEE Eng. Med. Biol. Soc.* **2010**, 4088-4091 (2010).
- 23 C. Timbó, L.A.R. da Rosa, M. Gonçalves, and S.B. Duarte, "Computational cancer cells identification by fractal dimension analysis," *Comput. Phys. Commun.* **180**, 850-853 (2009).
- 550 24 R. Lopes and N. Betrouni, "Fractal and multifractal analysis: A review," *Med. Image Anal.* **13**, 634-649 (2009).
- 25 V. Goh, B. Sanghera, D. Wellsted, J. Sundin, and S. Halligan, "Assessment of the spatial pattern of colorectal tumour perfusion estimated at perfusion CT using two-dimensional fractal analysis," *Eur. Radiology* **19**, 1358-1365 (2009).
- 555 26 B. Sanghera, D. Banerjee, A. Khan, I. Simcock, J.J. Stirling, R. Glynne-Jones, and V. Goh, "Reproducibility of 2D and 3D fractal analysis techniques for the assessment of spatial heterogeneity of regional blood flow in rectal cancer," *Radiology* **263**, 865-873 (2012).
- 27 N. Sarkar and B.B. Chaudhuri, "An efficient differential box-counting approach to compute fractal dimension of image," *IEEE Trans. Sys. Man Cyber.* **24**, 115-120 (1994).
- 560 28 D. Lv, X. Guo, X. Wang, J. Zhang, and J. Fang, "Computerized characterization of prostate cancer by fractal analysis in MR images," *J. Magn. Reson. Imaging* **30**, 161-168 (2009).
- 29 S. Kido, K. Kuriyama, M. Higashiyama, T. Kasugai, and C. Kuroda, "Fractal analysis of internal and peripheral textures of small peripheral bronchogenic carcinomas in thin-section computed tomography: comparison of bronchioloalveolar cell carcinomas with nonbronchioloalveolar cell carcinomas," *J. Comput. Assist. Tomogr.* **27**, 56-61 (2003).
- 565 30 A. Dimitrakopoulou-Strauss, L.G. Strauss, T. Heichel, H. Wu, C. Burger, L. Bernd, and V. Ewerbeck, "The role of quantitative (18)F-FDG PET studies for the differentiation of malignant and benign bone lesions," *J. Nucl. Med.* **43**, 510-518 (2002).
- 31 K. Falconer, *Techniques in Fractal Geometry*. (John Wiley & Sons. , Chichester, 1997).
- 570 32 I. Polycarpou, C. Tsoumpas, and P.K. Marsden, "Analysis and comparison of two methods for motion correction in PET imaging," *Med. Phys.* **39**, 6474-6483 (2012).
- 33 C. Tsoumpas, C. Buerger, A.P. King, P. Mollet, V. Keereman, S. Vandenberghe, V. Schulz, P. Schleyer, T. Schaeffter, and P.K. Marsden, "Fast generation of 4D PET-MR data from real dynamic MR acquisitions," *Phys. Med. Biol.* **56**, 6597-6613 (2011).
- 575 34 C. Tsoumpas, I. Polycarpou, K. Thielemans, C. Buerger, A.P. King, T. Schaeffter, and P.K. Marsden, "The effect of regularization in motion compensated PET image reconstruction: a realistic numerical 4D simulation study," *Phys. Med. Biol.* **58**, 1759-1773 (2013).

## Willaime *et al*: Space-filling index and PET quantification

- 35 K. Thielemans, C. Tsoumpas, S. Mustafovic, T. Beisel, P. Aguiar, N. Dikaios, and M.W. Jacobson, "STIR: software for tomographic image reconstruction release 2," *Phys. Med. Biol.* **57**, 867 (2012).
- 580 36 L.M. Kenny, D.M. Vigushin, A. Al-Nahhas, S. Osman, S.K. Luthra, S. Shousha, R.C. Coombes, and E.O. Aboagye, "Quantification of cellular proliferation in tumor and normal tissues of patients with breast cancer by F-18 fluorothymidine-positron emission tomography imaging: Evaluation of analytical methods," *Cancer Res.* **65**, 10104-10112 (2005).
- 585 37 L. Kenny, R.C. Coombes, D.M. Vigushin, A. Al-Nahhas, S. Shousha, and E.O. Aboagye, "Imaging early changes in proliferation at 1 week post chemotherapy: a pilot study in breast cancer patients with 3'-deoxy-3'-[18F]fluorothymidine positron emission tomography," *Eur. J. Nucl. Med. Mol. Imaging* **34**, 1339-1347 (2007).
- 38 J.M.Y. Willaime, F.E. Turkheimer, L.M. Kenny, and E.O. Aboagye, "Quantification of intra-tumour cell proliferation heterogeneity using imaging descriptors of 18F fluorothymidine-positron emission tomography," *Phys. Med. Biol.* **58**, 187 (2013).
- 590 39 N. Boussion, M. Hatt, F. Lamare, Y. Bizais, A. Turzo, C. Cheze-Le Rest, and D. Visvikis, "A multiresolution image based approach for correction of partial volume effects in emission tomography," *Phys. Med. Biol.* **51**, 1857-1876 (2006).
- 40 N. Boussion, C. Cheze Le Rest, M. Hatt, and D. Visvikis, "Incorporation of wavelet-based denoising in iterative deconvolution for partial volume correction in whole-body PET imaging," *Eur. J. Nucl. Med. Mol. Imaging* **36**, 1064-1075 (2009).
- 595 41 S.G. Chang, Y. Bin, and M. Vetterli, "Adaptive wavelet thresholding for image denoising and compression," *IEEE Trans. Image Process.* **9**, 1532-1546 (2000).
- 42 J. Mertens, A. Dobbeleir, H. Ham, Y. D'Asseler, I. Goethals, and C. Van de Wiele, "Standardized added metabolic activity (SAM): a partial volume independent marker of total lesion glycolysis in liver metastases," *Eur. J. Nucl. Med. Mol. Imaging* **39**, 1441-1448 (2012).
- 600 43 D. Visvikis, M. Hatt, F. Tixier, and C. Cheze Le Rest, "The age of reason for FDG PET image-derived indices," *Eur. J. Nucl. Med. Mol. Imaging* **39**, 1670-1672 (2012).
- 44 P. Cheebsumon, M. Yaqub, F. H. P. van Velden, O. S. Hoekstra, A. A. Lammertsma and R. Boellaard, "Impact of <sup>18</sup>F-FDG PET imaging parameters on automatic tumour delineation: need for improved tumour delineation methodology," *Eur. J. Nucl. Med. Mol. Imaging*, **38**, 2136–2144 (2011).
- 605 45 P. Cheebsumon, F.H.P. van Velden, M. Yaqub, V. Frings, A.J. de Langen, O.S. Hoekstra, A.A. Lammertsma, and R. Boellaard, "Effects of image characteristics on performance of tumor delineation methods: a test-retest assessment," *J. Nucl. Med.* **52**, 1550-1558 (2011).
- 46 C. Atupelage, H. Nagahashi, M. Yamaguchi, T. Abe, A. Hashiguchi, and M. Sakamoto, "Classification of Prostate Histopathology Images Based on Multifractal Analysis," *IEICE Trans.* **95-D**, 3037-3045 (2012).
- 610 47 J.W. Baish and R.K. Jain, "Fractals and cancer," *Cancer Res.* **60**, 3683-3688 (2000).
- 48 M. Hatt, C. Cheze le Rest, A. Turzo, C. Roux, and D. Visvikis, "A Fuzzy Locally Adaptive Bayesian Segmentation Approach for Volume Determination in PET," *IEEE Trans. Med. Imaging* **28**, 881-893 (2009).
- 615 49 M. Hatt, C. Cheze le Rest, E.O. Aboagye, L.M. Kenny, L. Rosso, F.E. Turkheimer, N.M. Albarghach, J.-P. Metges, O. Pradier and D. Visvikis, "Reproducibility of <sup>18</sup>F-FDG and 3'-Deoxy-3'-<sup>18</sup>F-Fluorothymidine PET Tumor Volume Measurements," *J. Nucl. Med.* **51**, 1368-1376 (2010).